Electronic Supplementary Information

Tin(II) Thiocyanate $Sn(NCS)_2$ – a Wide Band Gap Hole-Transporting Coordination Polymer Semiconductor

Chayanit Wechwithayakhlung,[a] Daniel M. Packwood,[b] Jidapa Chaopaknam,[a] Pimpisut Worakajit,[a] Somlak Ittisanronnachai,[c] Narong Chanlek,[d] Vinich Promarak,[ae] Kanokwan Kongpatpanich,[ae] David J. Harding[f] and Pichaya Pattanasattayavong[*ae]

[a]Department of Materials Science and Engineering, School of Molecular Science and Engineering, Vidyasirimedhi Institute of Science and Technology (VISTEC), Rayong, 21210, Thailand.

[b]Institute for Integrated Cell-Material Sciences (iCeMS), Kyoto University, Kyoto, 606-8501, Japan

[c]Frontier Research Center (FRC), Vidyasirimedhi Institute of Science and Technology (VISTEC), Rayong, 21210, Thailand

[d]Synchrotron Light Research Institute (Public Organization), 111 University Avenue, Muang District, Nakhon Ratchasima, 30000, Thailand

[e]Research Network of NANOTEC-VISTEC on Nanotechnology for Energy, Vidyasirimedhi Institute of Science and Technology (VISTEC), Rayong, 21210, Thailand

[f]Functional Materials and Nanotechnology Centre of Excellence (FuNTech), Walailak University, Nakhon Si Thammarat, 80160, Thailand

*Corresponding author's email: pichaya.p@vistec.ac.th

Note S1. $Sn(NCS)_2$ crystal structure

Product synthesis

White solids of $Sn(NCS)_2$ precipitated out upon the addition of the $Sn(SO_4)$ solution in diluted sulfuric acid into an aqueous solution of NaSCN. Keeping the solution at a low temperature (−20 °C) further promoted the crystallization. After the filtration and drying steps, white powder consisting of thin needles with lengths up to several mm, a form which is similar to reports by Chamberlain and Moser[1] and Filby et al.,[2] was collected (Fig. S1a). Observation of the solids under an optical microscope (Fig. S1b) reveals that the needles are composed of microscale crystals, several of which also exist as single crystals with lengths up to a hundred μm and widths of tens of μm.

Bond angle distortions and Sn···S contacts

The Sn–N1–C1 angle is 146.5° while the Sn–S1–C1 angle is smaller at 104.0°. The latter (Sn–S1–C1) follows the general metal–SCN bonding in which the S atom bonds through the π-MO of the thiocyanate and typically has a metal (M)–ligand (L) angle around 100°.[3–5] However, bonding with the N (Sn–N1–C1) generally occurs via a σ interaction and is expected to have a linear M–L angle, between 160-180°.[3–5] For example, the SCN unit in the 1D chain of the copper(I) thiocyanate-dimethyl sulfide complex $[Cu(SCN)(CH_3\text{-}S\text{-}CH_3)_2]_n$ has an N-bonded angle of 170.5° and an S-bonded angle of 96.4°.[6] It should also be noted that the angle $S1^{i}$–Sn–N1 of $Sn(NCS)_2$ is rather sharp at 73.0° compared to the angle S1–Cu–N1 of 106.7° in $[Cu(SCN)(CH_3\text{-}S\text{-}CH_3)_2]_n$. The acute $S1^{i}$–Sn–N1 angle and the significant deviation in the Sn–N1–C1 angle from linear in $Sn(NCS)_2$ are ascribed to the interchain linkage by the Sn···S contacts. The Sn···$S2^{ii}$ and Sn···$S2^{iii}$ interactions that link the 1D chains into 1D ribbons pull the Sn atoms on the chain closer toward the shared $S2^{ii}$ or $S2^{iii}$ contacts, resulting in the bending of the N-bonded bridging NCS (Fig. S2) and the acute $S1^{i}$–Sn–N1 angle as described above. Such effects on the main backbone suggest that these interactions play an important role in the $Sn(NCS)_2$ structure.

For the monocapped octahedral geometry of Sn (Fig. 1b in the main text), the three covalently bonded atoms (N1, N2, and $S1^{i}$) constitute the bottom trigonal face while the three S contacts ($S2^{ii}$, $S2^{iii}$, and $S1^{iv}$) form the top trigonal face on which the lone pair of Sn(II) is expected to occupy the capping position. The angles of the bottom trigonal pyramid (with Sn at the apex) are all acute while those of the top trigonal pyramid are all obtuse (Table S2).

Note S2. Crystallographic planes and *d*-spacing values from HRTEM image

The *d*-spacings of individual crystallites in Fig. 2e have been measured to have values between 2.65 to 3.31 Å. Within this narrow range, there are 12 possible crystallographic

planes due to the crystal structure of $Sn(NCS)_2$ (associated with diffractions with 2θ in the range of 26.9° to 33.8° in the PXRD spectrum). We therefore refrain from assigning planes to these *d*-spacings as the uncertainties from determining the *d*-spacing values from the HRTEM images (taking an average spacing value from the histogram of the marked area, examples shown in Fig. S4f-i) are estimated to be up to ±0.05 Å which is on the same order or larger than the differences between the *d*-spacings of these 12 planes. The planes of these nanocrystalline domains are also observed in the selected area electron diffraction (SAED) pattern as an unlabeled diffuse ring in Fig. 2g in the main text.

Note S3. Application of $Sn(NCS)_2$ as a hole transport layer in organic photovoltaics

OPV cell fabrication

The fabrication steps for the organic photovoltaic (OPV) cells are based on the procedure described in the literature.[7] Indium tin oxide (ITO)-coated glass substrates (150-nm ITO) were first patterned using negative dry film photoresist which was exposed to UV light and removed by 1% NaOH solution. The unprotected ITO area was etched using aqua regia to realize the patterned anode of the cells. The patterned ITO substrates were cleaned with detergent, de-ionized (DI) water, acetone, and isopropyl alcohol (IPA) then dried with N_2 and treated with UV-ozone to improve the wettability. $Sn(NCS)_2$ as the hole transport layer (HTL) was spin-coated onto the patterned ITO substrates at 2000 rpm from a 20 mg mL^{-1} solution of $Sn(NCS)_2$ in ethanol and left to dry under N_2 atmosphere at room temperature. For the reference cell, poly(3,4-ethylenedioxythiophene) polystyrene sulfonate (PEDOT:PSS) was used as the HTL. The PEDOT:PSS dispersion (Clevios AI 4083, Heraeus) was spin-coated onto the patterned ITO substrates at 5000 rpm and annealed at 150 °C for 20 min under ambient air. The light-absorbing layer consisted of poly[4,8-bis(5-(2-ethylhexyl)thiophen-2-yl)benzo[1,2-b;4,5-b']dithiophene-2,6-diyl-alt-(4-(2-ethylhexyl)-3-fluorothieno[3,4-

b]thiophene-)-2-carboxylate-2-6-diyl)] (PTB7-Th; PCE10 M261, Ossila) as the donor and [6,6]-phenyl-C_{71}-butyric acid methyl ester ($PC_{70}BM$; 99%, Ossila) as the acceptor forming the PTB7-Th:$PC_{70}BM$ bulk heterojunction (BHJ) layer (Fig. S8a). The solution containing PTB7-Th:$PC_{70}BM$ with a blend ratio of 1:1.5 in anhydrous chlorobenzene at a total concentration of 20 mg mL^{-1} and 3% 1,8-diiodooctane (DIO) as an additive was spin-coated onto the HTL at 1750 rpm under N_2 atmosphere. This step was immediately followed by dropping a small amount of methanol (while still spinning) to remove DIO. The active layer was left to dry under N_2 atmosphere at room temperature. Finally, 10-nm of bathocuproine (BCP) and 100-nm of Al, which were employed as the electron transport layer (ETL) and the cathode, respectively, were deposited using thermal evaporation through a shadow mask. The schematic cross-section of the cell structure is shown in Fig. S8b. The thicknesses of the spin-coated layers were measured by a profilometer (Bruker DektakXT) as: PEDOT:PSS = 36 nm, $Sn(NCS)_2$ = 30 nm, and BHJ = 50 nm.

OPV cell characterization

The electrical characterization of the OPV cells was performed with a source meter (Keithley 2400) under simulated sunlight (Newport 96000 with AM1.5G filter) and ambient atmosphere. The illumination intensity was calibrated to 100 mW cm^{-2} with a Si photodiode (Bunkoukeiki BS-520). The active area of each OPV cell was a circular area of 0.181 cm^2.

OPV results and discussion

Fig. S8c shows the current density-voltage (*J*-*V*) characteristics of the fabricated OPVs. Employing $Sn(NCS)_2$ as the HTL yielded working OPV cells, confirming that $Sn(NCS)_2$ can function as a hole-transporting semiconductor. Table S3 reports the operating parameters of $Sn(NCS)_2$-based OPV cells, including the values averaged from five cells, the errors calculated from the standard deviation, and the parameters of the best performing cell. The values of the reference cell with PEDOT:PSS as the HTL are also listed for comparison. At

this point, the performance of the cells with $Sn(NCS)_2$ as the HTL is still inferior to that of the reference cell since the processing and the properties of the $Sn(NCS)_2$ film have not been optimized. One of the main issues is the rapid crystallization or agglomeration of $Sn(NCS)_2$ upon solvent evaporation that results in the formation of inhomogeneous, discontinuous film as shown in Fig. S8d. The poor film quality consequently leads to the low fill factor (FF) and power conversion efficiency (PCE), especially for cells with a relatively large area of 0.181 cm^2. Nevertheless, this is a successful demonstration of the application of $Sn(NCS)_2$ as a hole-transporting material and suggests that there is plenty of room for optimization. Indeed, this is the subject of our ongoing investigation. A smooth and uniform HTL is expected to significantly increase the cell performance.[7]

References

1 B. R. Chamberlain and W. Moser, *J. Chem. Soc. A Inorganic, Phys. Theor.*, 1969, **500**, 354.

2 A. G. Filby, R. A. Howie and W. Moser, *J. Chem. Soc. Dalt. Trans.*, 1978, **3**, 1797.

3 L. Di Sipio, L. Oleari and G. De Michelis, *Coord. Chem. Rev.*, 1966, **1**, 7–12.

4 R. R. da Silva, J. M. Santos, T. C. Ramalho and J. D. Figueroa-Villar, *J. Braz. Chem. Soc.*, 2006, **17**, 223–226.

5 C.-H. Hsieh, S. M. Brothers, J. H. Reibenspies, M. B. Hall, C. V. Popescu and M. Y. Darensbourg, *Inorg. Chem.*, 2013, **52**, 2119–2124.

6 G. Ayala and R. D. Pike, *Polyhedron*, 2016, **115**, 242–246.

7 N. Wijeyasinghe, A. Regoutz, F. Eisner, T. Du, L. Tsetseris, Y.-H. Lin, H. Faber, P. Pattanasattayavong, J. Li, F. Yan, M. A. McLachlan, D. J. Payne, M. Heeney and T. D. Anthopoulos, *Adv. Funct. Mater.*, 2017, **27**, 1701818.

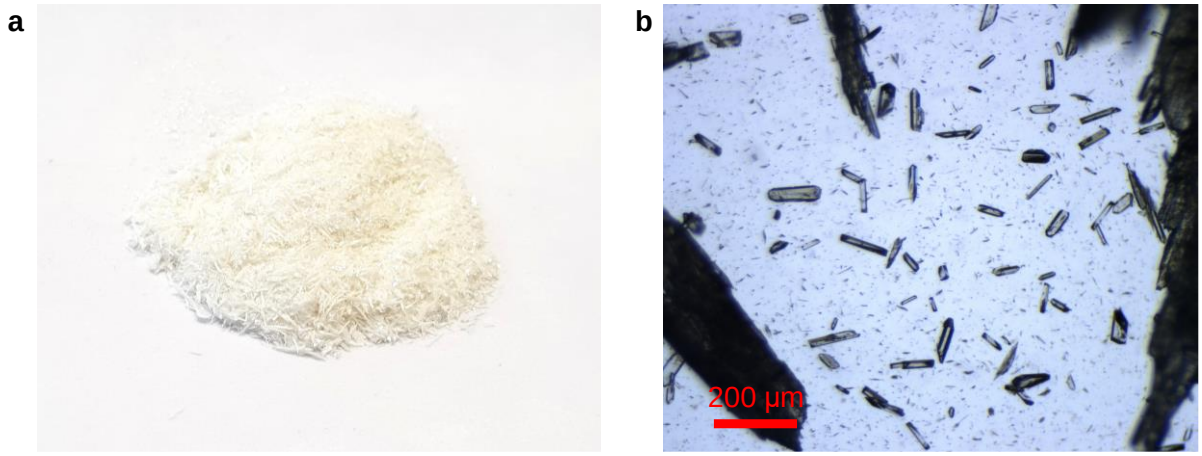

Fig. S1 (a) Bulk sample of $Sn(NCS)_2$ obtained after synthesis. Lustrous white needles are visible. (b) $Sn(NCS)_2$ sample under optical microscope. Some particles are single crystals which were used for single crystal X-ray measurement and analysis.

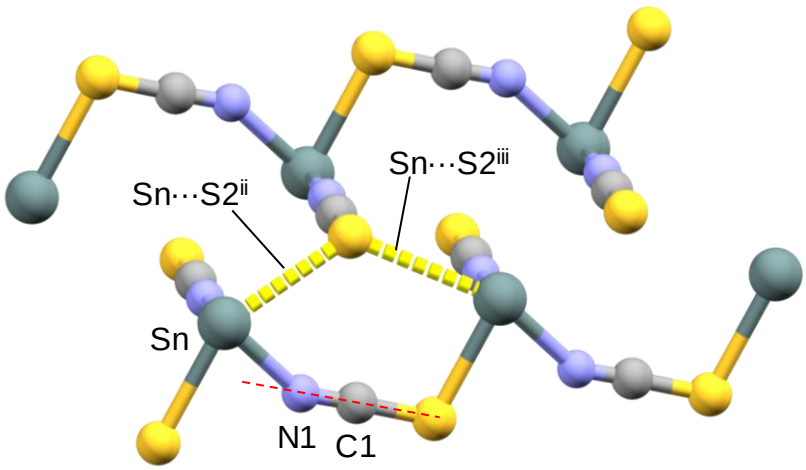

Fig. S2 Significant non-covalent Sn···S interactions (Sn···S2^{ii} and Sn···S2^{iii} contacts) that form the interchain linkage joining two centrosymmetric 1D chains into a 1D ribbon. The contacts pull the Sn atoms toward the shared S causing the angle Sn–N1–C1 to deviate from linear to 146.5°.

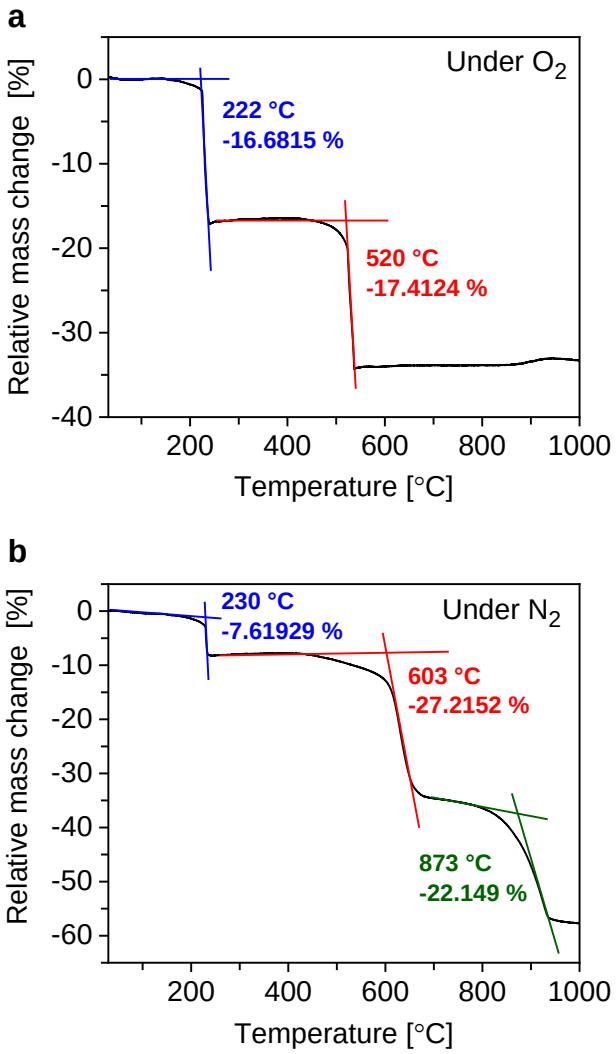

Fig. S3 Plots of relative mass changes of $Sn(NCS)_2$ powder samples from thermogravimetric measurements under (a) O_2 and (b) N_2.

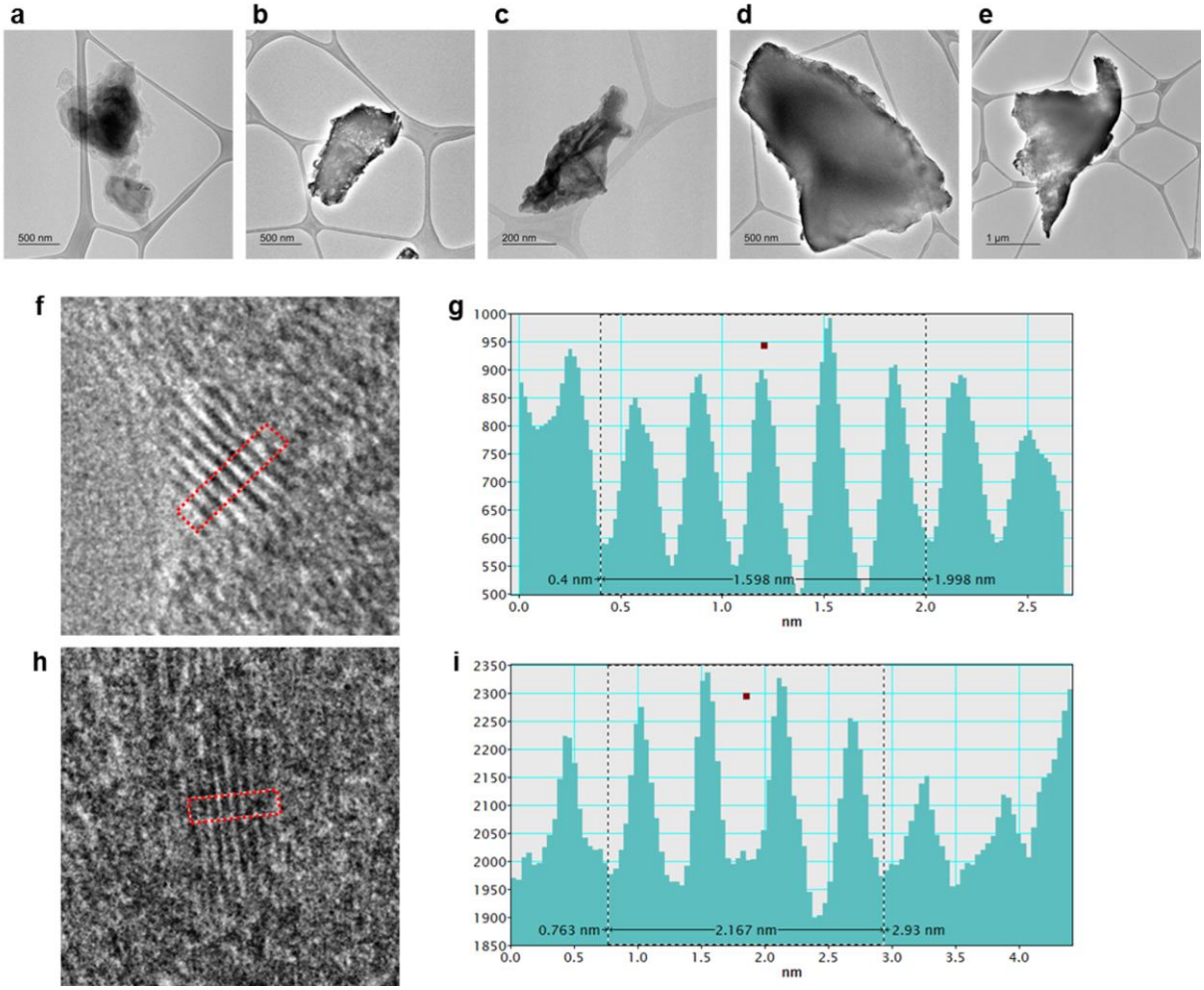

Fig. S4 (a)-(e) TEM images of different $Sn(NCS)_2$ flakes. A layered structure can be observed, especially near the edges of the flakes. The web-like structures in the background are lacey carbon support. (f) HRTEM image of a nanocrystalline grain similar to Fig. 2e in the main text. The dashed red box marks the area selected to calculate the *d*-spacing. (g) Histogram of the dotted red box in (f). The *d*-spacing is calculated from the average distance, in this case, of five fringes. (h) and (i) are the same as (f) and (g) but of a nanocrystalline grain similar to Fig. 2f in the main text.

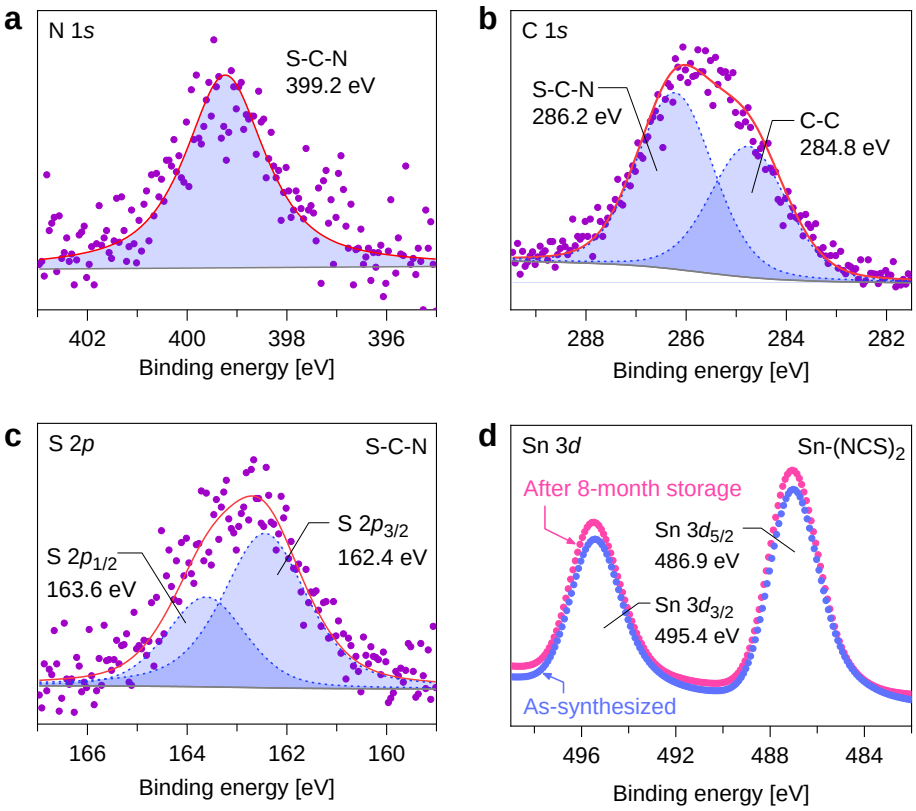

Fig. S5 (a), (b), and (c) Core-level XPS spectra of N 1*s*, C 1*s*, and S 2*p*, respectively, of $Sn(NCS)_2$ powder sample. Scattered points are collected data. Solid gray line is the background. Dashed blue line and the corresponding blue-shaded region show the fitted peak. Solid red line is the reconstructed spectrum from the fitted peaks. Spectra of N, C, and S are assigned to NCS ligand. (d) The comparison of the Sn 3*d* XPS spectra of a freshly prepared sample (violet circles) and an aged sample which had been stored for 8 months under air at room temperature and relative humidity of 30% (pink circles). No differences in the chemical state can be observed, further corroborating the stability of $Sn(NCS)_2$.

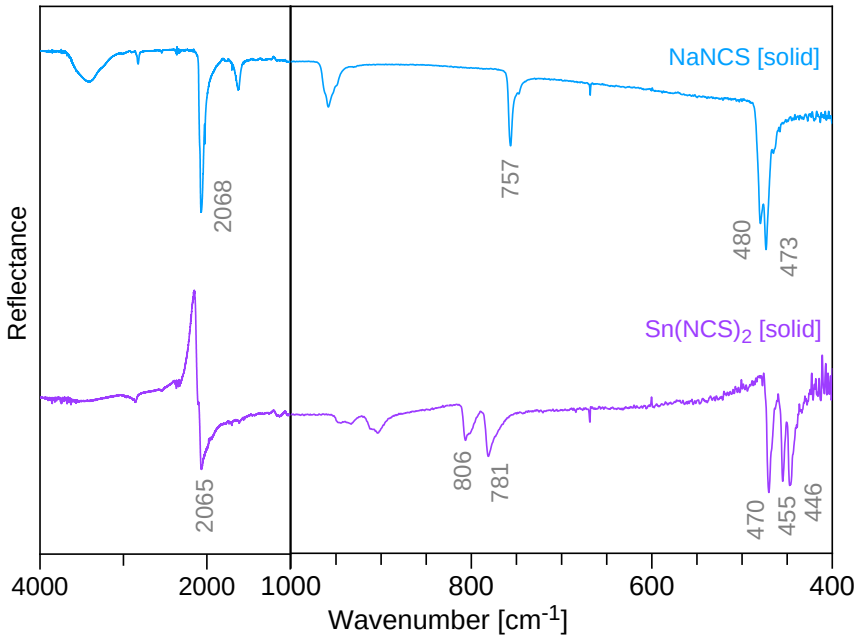

Fig. S6 Reflectance spectra of $Sn(NCS)_2$ sample and NaSCN (thiocyanate source in the synthesis) measured with ATR-FTIR.

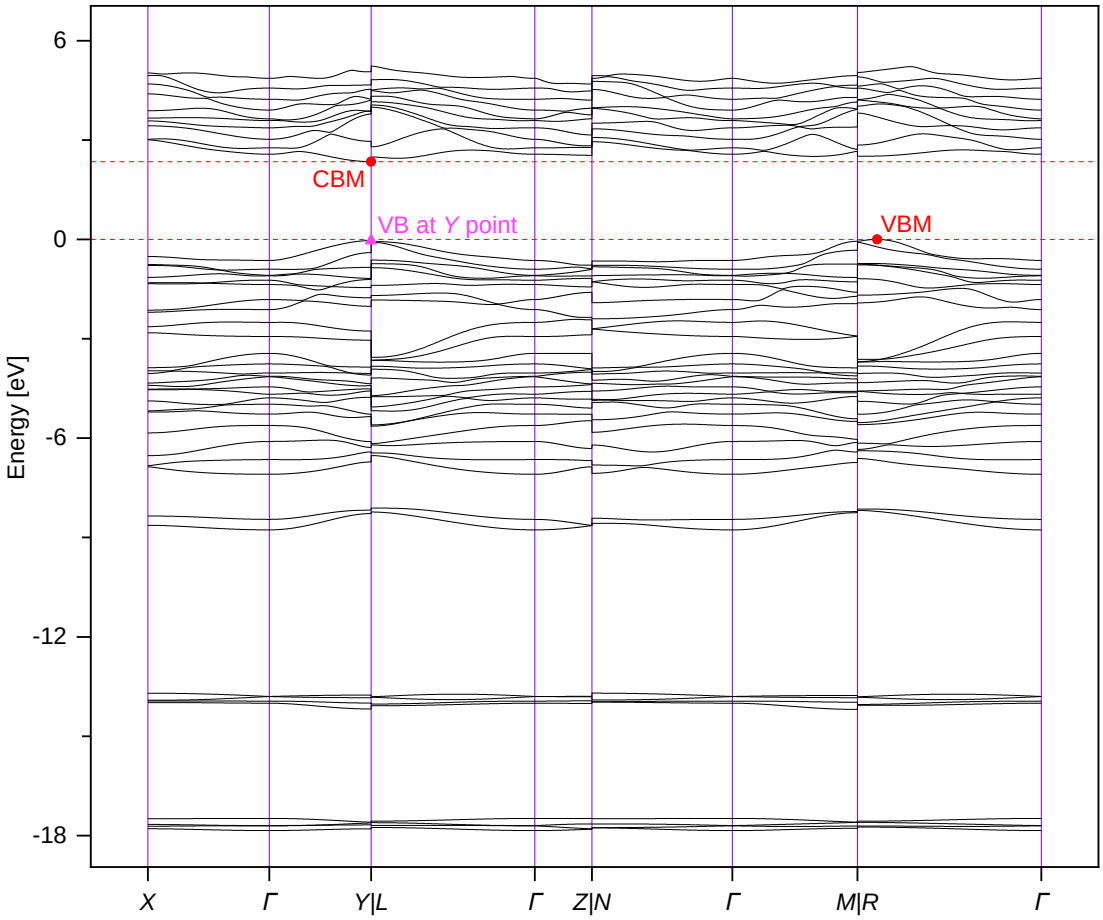

Fig. S7 Electronic band structure of $Sn(NCS)_2$ calculated with DFT. The valence band maximum (VBM) and conduction band minimum (CBM) (solid red circles) occur at different *k*-points. Their energy difference, which in this case corresponds to the fundamental indirect band gap, is 2.35 eV. Also, the VB at *Y* point (solid pink triangle) is only 0.3 eV lower in energy than the VBM, resulting in a direct band gap of 2.38 eV.

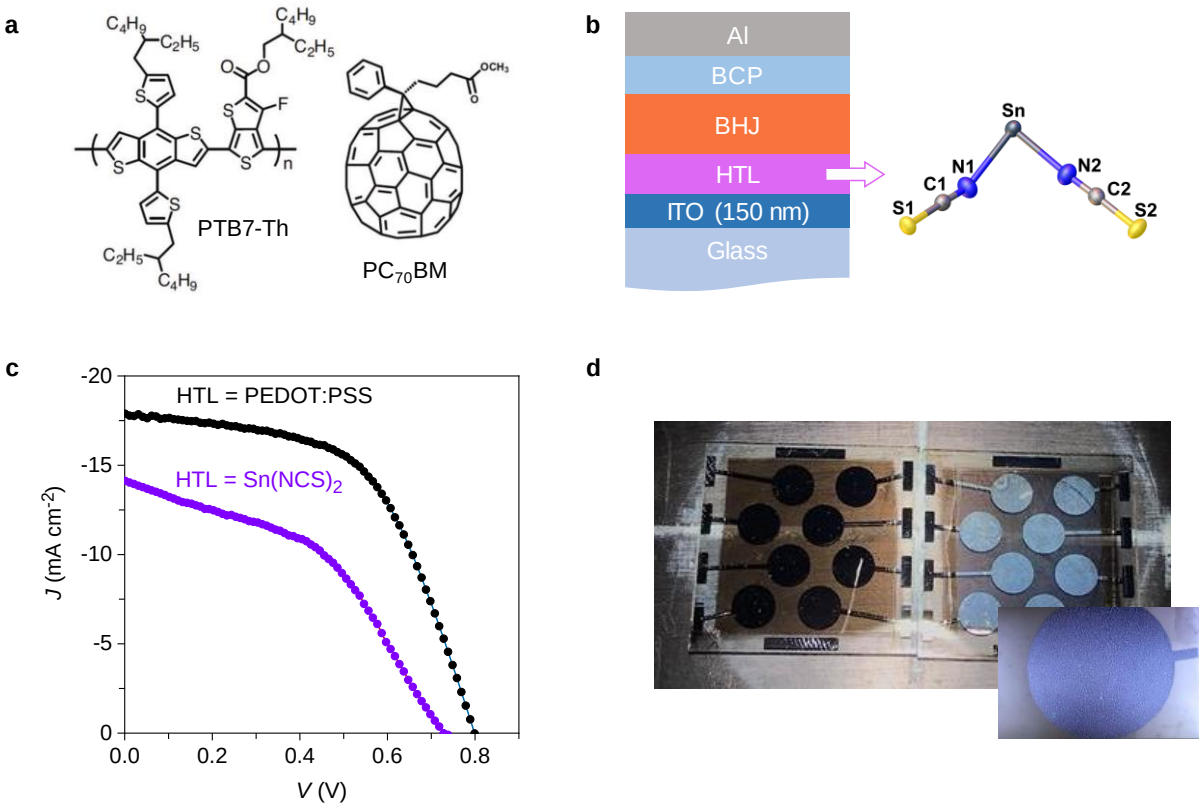

Fig. S8. (a) Chemical structures of PTB7-Th and $PC_{70}BM$ employed as the donor and acceptor, respectively, for the active BHJ layer of the OPV cells. (b) Schematic diagram of the cross-section of the fabricated OPV cells. $Sn(NCS)_2$ was used as the HTL. For a reference cell, PEDOT:PSS was used as the HTL. (c) *J-V* characteristics of the best performing cell with $Sn(NCS)_2$ as the HTL (PCE = 4.55%) and the reference cell with PEDOT:PSS as the HTL (PCE = 8.01%). (d) Photographs of the fabricated OPV cells with PEDOT:PSS (left) and $Sn(NCS)_2$ (right) as the HTL. Cells based on $Sn(NCS)_2$ appear white due to light scattering as a result of the rough and inhomogeneous $Sn(NCS)_2$ film which rapidly crystallized upon solvent evaporation (inset).

Table S1 Bond/contact lengths in angstroms [Å].

Bridging thiocyanate	
S1–C1	1.642(2)
C1–N1	1.161(3)
Terminal thiocyanate	
S2–C2	1.631(2)
C2–N2	1.162(2)
Sn coordination	
Sn–N2	2.198(2)
Sn–N1	2.283(2)
Sn–S1^{i}	2.8208(4)
Sn···S2^{ii}	3.1292(5)
Sn···S2^{iii}	3.3086(5)
Sn···S1^{iv}	3.5004(5)

The superscripts indicate the following symmetry labels:
i = $+x, -1+y, +z$
ii = $1-x, 1-y, 1-z$
iii = $1-x, -y, 1-z$
iv = $1-x, 1-y, -z$

Table S2 Bond/contact angles in degrees [°]

Bridging thiocyanate	
N1–C1–S1	177.8(2)
Terminal thiocyanate	
N2–C2–S2	177.9(2)
Sn–NCS *bond/contact angle*	
with respect to longitudinal axis of NCS	
Sn–N2–C2	175.5(1)
Sn–N1–C1	146.5(2)
Sn–S1^{i}–C1^{i}	104.03(6)
Sn···S2^{ii}–C2^{ii}	99.22(6)
Sn···S2^{iii}–C2^{iii}	98.10(6)
Sn···S1^{iv}–C1^{iv}	103.43(6)
Tetrel bond angle	
S1^{i}–Sn···S2^{ii}	146.41(1)
N1–Sn···S2^{iii}	155.05(5)
N2–Sn···S1^{iv}	151.75(4)
Bottom trigonal pyramid	
N1–Sn–S1^{i}	73.02(5)
S1^{i}–Sn–N2	85.33(4)
N2–Sn–N1	83.28(6)
Top trigonal pyramid	
S2^{ii}···Sn···S2^{iii}	123.42(1)
S2^{iii}···Sn···S1^{iv}	113.97(1)
S1^{iv}···Sn···S2^{ii}	104.40(1)

The superscripts indicate the following symmetry labels:
i = $+x, -1+y, +z$
ii = $1-x, 1-y, 1-z$
iii = $1-x, -y, 1-z$
iv = $1-x, 1-y, -z$

Table S3 Summary of the device parameters of OPV cells employing reference PEDOT:PSS or $Sn(NCS)_2$ as the HTL.

HTL	J_{sc} (mA cm^{-2})	V_{oc} (V)	FF	PCE (%)
Reference PEDOT:PSS	17.88	0.80	0.56	8.01
$Sn(NCS)_2$	14.18 ±1.12 (14.13)	0.73 ±0.05 (0.73)	0.39 ±0.03 (0.44)	4.06 ±0.29 (4.55)

The reported values of OPVs with $Sn(NCS)_2$ HTL are averaged from five cells. The errors are calculated from the standard deviation. The values given in the brackets are those of the champion cell. J_{sc} = short-circuit current, V_{oc} = open-circuit voltage, FF = fill factor, and PCE = power conversion efficiency.